RSC Advances

ROYAL SOCIETY OF CHEMISTRY

www.rsc.org/advances

Journal Name

RSCPublishing

ARTICLE

Chromium oxide coated nickel/yttria-stabilized zirconia electrode with heterojunction interface toward electrochemical methane reforming

Wentao Qi,[a] Shigang Chen,[a] Yucheng Wu,[a] Kui Xie,[a, b] *

Cite this: DOI: 10.1039/x0xx00000x

Received 00th January 2012,
Accepted 00th January 2012

DOI: 10.1039/x0xx00000x

www.rsc.org/

This work investigates the nickel/yttria-stabilized zirconia (Ni/YSZ) *in-situ* coated with chromium oxide for electrochemical methane reforming in solid oxide electrolysers. Combined analysis using XRD, TEM, SEM and XPS confirm the formation of Cr_2O_3 on Ni surface with heterojunction interface through reducing formed $NiCr_2O_4$ a core-shell structure. The electrical properties of Cr_2O_3-coated Ni/YSZ are investigated and correlated to electrochemical performances. Significant improvements on electrode activity have been achieved with Cr_2O_3-coated Ni/YSZ in contrast to traditional Ni/YSZ in methane atmosphere. Strong carbon deposition resistance has also been observed in CH_4-CO_2 (1:1) atmosphere at 800 °C. Significant enhancement in Electrochemical CH_4-CO_2 reforming is successfully achieved in oxide-ion-conducting electrolysers with Cr_2O_3-coated Ni/YSZ cathodes.

Introduction

There has been increasing global concern over the rise of CO_2 emissions into the earth's atmosphere in which the increasing concentrations of CO_2 and CH_4 play an important role in raising the global temperature [1-4]. Therefore, there has been increased interest in a better understanding of CO_2 and CH_4 removal, disposal and utilization. Methane reforming with carbon dioxide produces synthesis gas with a lower H_2/CO ratio, which is desirable for the production of higher hydrocarbons and oxygenated derivatives. This reaction also has important environmental implications since both CH_4 and CO_2 are greenhouse gases [5-8]. So far, most methane reforming is preferentially performed using heterogeneous catalysts, for instance, transition metal oxides loaded with metal nanocatalysts at low temperatures [9-10]. The CH_4 or CO_2 activation is reported through chemical adsorption on surface defect sites or the thermal spitting of CH_4 on the surface of metal catalysts. Theoretical investigations of CH_x species adsorbed on Pt (111) and Rh (111) indicate that CH_x fragments are preferentially located at a site on the metal surface [11-12]; the stepwise decomposition of CH_4 into CH_x fragments on a metal surface can benefit the catalysis conversion. On the other hand, the chemisorption and dissociation of CO_2 on the metal surface may be beneficial for dry CO_2 reforming of CH_4 [13-14].

Solid oxide electrolysers have been attracting widespread attentions because they are high efficient energy conversion devices to produce clean fuel through high-temperature electrolysis with favorable kinetics and thermodynamics [15-17]. The high temperature is favorable for improving direct internal reforming reactions of methane ($CH_4 + CO_2 \rightarrow 2CO + 2H_2$; $\Delta G° = 61770 - 67.32T$) to produce hydrogen and carbon monoxide in the cathode of the solid oxide electrolyser. The direct heat exchange between the exothermic electrochemical reactions and the endothermic reforming reactions is one of the main advantages of the direct internal reforming configuration which has potential to increase the overall system efficiency and minimize reforming components [18]. An oxide-ion-conducting solid oxide electrolyser can directly electrolyze carbon dioxide into carbon monoxide and oxygen [19-21]. Firstly, CO_2 molecules are split into active $CO^{\cdot}$ and $O^{\cdot}$, and then

electrochemically transformed to CO and O^{2-}, respectively. The O^{2-} ions are transported through electrolyte to anode where O_2 is formed and released. Irvine *et al.* have demonstrated the successful electrochemical conversion of CO_2-H_2O into syngas in an oxide-ion-conducting solid oxide electrolyser with $La_{0.2}Sr_{0.8}TiO_{3.1}$ cathode. The H_2O and CO_2 molecules can diffuse through the porous cathode to the triple phase boundary (TPB) at the cathode-electrolyte interface, where hydrogen species produced can react with produced CO or CO_2 directly giving rise to synthetic hydrocarbon fuels in the presence of appropriate metal catalysts [22]. As a consequence, the feature of CO_2 electrolysis makes it possible to *in situ* utilize $O^{\cdot}$ at the TPB to oxidize methane into syngas before it is transported to the anode under external applied voltages. On the other hand, the thermal splitting of CH_4 into CH_x fragments on the electrode surface is also in favor of the catalytic oxidation process.

The conventional Ni/YSZ composite electrode not only has been preferentially used as the cathode for oxide-ion-conducting solid oxide electrolysers, but also used as the anode of solid oxide fuel cells, which is attributed to its excellent catalytic property for the oxidation of hydrogen fuels and stability in solid oxide electrolysis cells (SOEC) or solid oxide fuel cells (SOFC) operation environment [23-26]. However, Ni/YSZ is not redox-stabe and requires a high concentration of reducing gas flowing over the Ni to avoid the oxidation of Ni to NiO [27-28]; besides, it will fail when hydrocarbon fuels are directly utilized due to the fact that Ni is an excellent catalyst for cracking hydrocarbon fuels, Ni decomposes the hydrocarbon fuels which form carbon on the electrode, that degrades cell performance and damages the electrode microstructures [29-30].

In order to prevent carbon deposition while operating the cell with hydrocarbon fuels, many strategies have been tried. Steam is the most commonly used oxygen carrier to avoid adverse reactions leading to carbon deposition on the electrode surface. However, a high steam partial pressure not only adds complexity to the system design and control, but also reduces the electrical efficiency of the system [31-32]. Carbon dioxide reforming is another interesting approach to avoid carbon deposition. Cosimo Guerra *et al.* performed high conversions of CH_4 ($CH_{4,rel.conv.}$ is always higher than 60% for $CO_2/CH_4 \geq 1$) and achieved no carbon formation when the molar ratio for the catalytic conversion of a mixture of CH_4 and CO_2 in H_2 and CO is $1.5 < CO_2/CH_4 < 2$ [33]. Compared with steam reforming, dry reforming can be employed in areas where steam is not available and it yields syngas with lower H_2/CO ratio, which is a preferable feedstock for the Fischer-Tropsch synthesis of long-chain hydrocarbon [34-35]. Many new materials have been studied for the substitutes of Ni/YSZ, such as doped $LaCrO_3$, doped $SrTiO_3$, Sr_2MgMoO_6 and so on [36-38]. Irvine *et al.* reported that $La_{0.75}Sr_{0.25}Cr_{0.5}Mn_{0.5}O_3$ (LSCM) electrode used for SOFC anode revealed comparable performances in H_2 compared with Ni/YSZ electrode and was active for wet CH_4 (3 mol% H_2O) oxidation at high temperatures [39]. We have recently demonstrated the successful electrochemical methane reforming in an oxide-ion-conducting solid oxide electrolyser with titanate cathode. Efficiently dry reforming of CH_4-CO_2 mixtures is successfully achieved in a thin-layer cathode under external electrical voltages [40]. Although the ceramic electrodes shows good promise for direct utilization of hydrocarbon fuels, the most used materials for the state-of-art SOFC or SOEC remains Ni/YSZ composite electrode which is attributed to Ni/YSZ has low cost, good electrochemical reactivity, high electrical conductivity and catalytic activity for reforming of hydrocarbon fuels at high temperatures.

The modification of Ni/YSZ can also improve carbon tolerance in the internal reforming of hydrocarbon fuels. The modification method includes replacing Ni by Ni-based alloy or other metals, the replacement of YSZ with Scandia-stabilized zirconia (ScSZ) and adding noble or rare earth metals into Ni/YSZ, etc. [41-45]. Gorte *et al.* demonstrated that the direct, electrocatalytic oxidation of methane can be achieved in SOFCs with Cu/CeO_2/YSZ anodes and carbon deposition does not occur on the Cu-based anodes [46]. They also reported that Co/CeO_2/YSZ composite was found to form large amounts of carbon upon expose to dry CH_4 at 800 ^oC for 3 h, the Co/Cu/CeO_2/YSZ composites did not form measurable amounts of carbon for the same conditions [47]. Liu *et al.* reported a new anode with nanostructured barium oxide/nickel (BaO/Ni) interfaces for low-cost SOFCs, demonstrating high density and stability in C_3H_8, CO and gasified carbon fuels at 750 ^oC. The results indicate that BaO helps to improve the carbon tolerance of Ni/YSZ electrodes [48]. However, BaO may diffuse into YSZ and lead to a high volume expansion in the YSZ grains which will cause delamination and cracking of YSZ layer. In addition, the diffusion of BaO in YSZ also blocks the O^{2-} transport and lowers the cell performances [49-50]. It is worth noting that the partial or full replacement of Ni by other metal elements lower the performances of the cermet electrode; on the other hand, the use of noble or rare earth metal is restricted by low cost for commercialization.

Therefore, it is necessary to find a new strategy to substantially modify traditional Ni/YSZ electrode and yields excellent stability with high catalytic activity for hydrocarbon oxidation. Chromium oxide has been widely utilized as an oxide catalyst with outstanding carbon deposition resistance properties in heterogeneous catalysis. Wang *et al.* reported that Cr_2O_3/SiO_2 is an effective catalyst for dehydrogenation of ethane and CO_2 in the feed promotes the catalytic activity [51]. El-Idrissi *et al.* studied the oxidative dehydrogenation of ethane over Cr_2O_3/TiO_2 and found the catalytic activity could be attributed to the isolated Cr^{3+} species on the support [52]. In this work, Cr_2O_3 is firstly impregnated in Ni/YSZ electrode to form $NiCr_2O_4$ and then reduced to *in situ* construct a core-shell structure with Ni metal core coated with Cr_2O_3 surface. The interface between Ni and oxide is systematically examined. Electrochemical methane reforming is then performed with this novel cathode in oxide-ion-conducting solid oxide electrolysers.

Experimental

All chemicals utilized in this current investigation were of analytical grade unless otherwise specified. All the powders were purchased from SINOPHARM Chemical Reagent Co., Ltd (China). The $NiCr_2O_4$ powders were prepared by a combustion method [53]. In the combustion method, appropriate molar ratios of $Cr(NO_3)_3{\cdot}9H_2O$, $Ni(NO_3)_2{\cdot}6H_2O$ and glycine were dissolved in a minimum volume of distilled water to obtain a transparent solution and stirred for a few minutes at 80 ^oC to get viscous gel. The glycine/nitrate stoichiometric molar ratio was 2.5/1. Then the viscous gel was transferred into a preheated furnace maintained at 500 ^oC for 5 minutes. The gel rapid burned and the green colour powders were obtained. In order to burn off carbon residues, the powders were further heated at 800 ^oC (3 ^oC min^{-1}) for 3 h in air. The $(La_{0.8}Sr_{0.2})_{0.95}MnO_{3-\delta}$ (LSM) was synthesized using the same method with the final heat treatment conducted at 1100 ^oC (3 ^oC min^{-1}) for 3 h in air. A part of $NiCr_2O_4$ powders were reduced in 5%H_2/Ar at 800 ^oC (3 ^oC min^{-1}) for 10 h for subsequent research.

The phase formation of oxidized and reduced $NiCr_2O_4$ powders was confirmed using X-ray diffraction (XRD, Cu Kα, $2\theta = 3^o{\cdot}min^{-1}$, D/MAX2500V, Rigaku Corporation, Japan) with 2θ ranging from 10º to 80º. The microstructures of the oxidized and reduced $NiCr_2O_4$ were investigated by Scanning Electron Microscopy (SEM, SU8020, HITACHI Ltd, Japan) coupled with Energy Dispersive Spectroscopy (EDS). The morphological features were examined by SEM images under high vacuum (10^{-6} mbar), at 20 kV accelerating voltage and 90μA beam current. These regions were then examined by EDS, using a liquid N_2-cooled Si(Li) detector with a super-ultrathin Be window. Spectra were collected from six regions per surface employing area scan mode under 20 kV accelerating voltage, 110 μA beam current and 500 s acquisition time. Transmission Electron Microscopy analysis (TEM, JEM-2100F,JEOL Ltd, Japan) was used to observe the oxidized and reduced $NiCr_2O_4$ powders with a JEOL 2100F field emission transmission electron microscope operated at 200 kV. X-ray photoelectron spectroscopy (XPS, ESCALAB25, Thermo, USA) was used to analyze the chemical states of the elements in the samples before and after high-temperature reduction. The valence states of the elements in the oxidized and reduced samples were determined using X-ray photoelectron spectroscopy (XPS) on a Thermo ESCALAB 250 with Al-Ka (1486.6 eV) radiation source. The binding energies were calibrated to the C1s peak at 285 eV.

About 2.0 g $NiCr_2O_4$ powders were pressed into a bar at a pressure of 5 MPa (20.0×7.0×2.4) followed by sintering at 1200 ^oC (3 ^oC min^{-1}) for 10 h in air to obtain samples for the conductivity tests. The conductivity was performed in air using the DC four-terminal method with temperature ranging from 200 to 800 ºC. The conductivity measurement was recorded versus temperature with an online system at a step 0.5 ^oC from room temperature to 800 ^oC. The dependence of conductivity on the oxygen partial pressure was tested at 800 ºC with the oxygen partial pressure ranging from 10^{-2} to 10^{-18} atm. The oxygen partial pressure that ranged from 10^{-2} to 10^{-18} atm was changed by flowing the dry 5%H_2/Ar at the flow rate of 0.5 mL min^{-1} controlled by a mass flow meter (D08-3F, Sevenstar, China) and recorded using an online oxygen sensor (Type 1231, ZrO_2-based oxygen sensor, Noveltech, Australia). The conductivity was recorded with an online multi-meter (Keithley 2000, Digital Multimeter, Keithley Instruments Inc., USA).

Electrolyte supported cells with two types of anode, designated as Ni/YSZ and 5% Cr_2O_3-Ni/YSZ, were fabricated in the present study. The 2-mm-thick 8YSZ electrolyte support was prepared by dry-pressing 8YSZ powders into a green disk at a pressure of 8 MPa with a diameter of 20 mm and thickness of 3mm followed by a sintering at 1500 ^oC (2 ^oC min^{-1}) for 20 h in air. The two surfaces of YSZ electrolyte support were mechanically polished and ultrasonically cleaned in ethanol and distilled water. The Ni/YSZ slurries were prepared by milling NiO and 8YSZ at a weight ratio of 60:40 in alpha-terpineol with appropriate amounts of cellulose

additives (approximately 10% weight ratio compared with the ceramic powders). The composite LSM/YSZ slurries were prepared by milling YSZ powders with LSM powders at a weight ratio of 35:65 in the alpha-terpineol with cellulose additive in a similar way. The symmetric electrolyzer was prepared by printing Ni/YSZ electrode slurry onto both surfaces of the YSZ electrolyte with an area of approximately 1 cm^2 followed by a heat treatment at 1400 ºC (3 $^oC\ min^{-1}$) for 3 h in air. The electrodes based on 5% Cr_2O_3-Ni/YSZ were prepared by infiltrating $Cr(NO_3)_3$ solution (0.5 mol L^{-1}) followed by a heat treatment at 1000 ºC (5 $^oC\ min^{-1}$) for 3 h in air. The impregnation-calcination process was repeated for two cycles to get 5% Cr_2O_3-Ni/YSZ compositions. Silver paste (SS-8060, Xinluyi, Shanghai, China) was printed on both surfaces of the electrodes as the current collector layers. The external circuit was made with silver wire (0.4 mm in diameter) which was fastened to current collectors using conductive adhesive (DAD87, Shanghai Research Institute for Synthetic Resins, Shanghai, China) followed by firing at 550 ºC (3 $^oC\ min^{-1}$) for 30 min in air. The symmetrical cells were tested at the open circuit voltage (OCV) in different hydrogen or methane partial pressure at 800 ^oC using the electrochemical workstation (IM6, Zahner, Germany) with a frequency range of 4 MHz–0.1 Hz in a two-electrode mode. The electrode polarization resistance was calculated by modeling the spectra using Zview software. The hydrogen partial pressure and methane partial pressure were changed by adjusting the gas flow rates of H_2 (99.99%), CH_4 (99.99%) and Ar (99.999%) using a mass flow meter (D08-3F, Sevenstar, China) while the total flow rate was maintained at 20 mL min^{-1}. The single solid oxide electrolyzers with LSM/YSZ anode were prepared in the same way, as discussed above. The single solid oxide electrolyzers were sealed to a home-made testing jig using ceramic paste (JD-767, Jiudian, Dongguan, China) for electrochemical measurements. The electrochemical measurements, including the AC impedance and current–voltage (*I–V*) plot of the solid oxide electrolyzer, were performed with the cathode electrode exposed to flowing 20% CH_4/20% CO_2/60% Ar and the oxygen electrode in static air at 800 ^oC. The gas flow rate was maintained at 30 mL min^{-1} using mass flow meters. The methane reforming was performed at different applied voltages with 20% CH_4/20% CO_2/60% Ar fed into fuel electrode at 800 ^oC. The output gas from cathode was analyzed using an online gas chromatograph (GC9790II, Fuli, Zhejiang, China) equipped with 10 m molecular sieve 5A (MS5A) column for the detection of hydrogen, carbon monoxide, methane and other noble gases. The column temperature was set at 50 ^oC and programmed to rise at 5 ^oC/min to 80 ^oC. Some tests were repeated in order to check for reproducibility. The maximum errors for both conversion and production were <1%.

Results and discussion

The XRD patterns of the Ni/YSZ, chromium oxide-loaded Ni/YSZ and $NiCr_2O_4$ are shown in Fig. 1. Fig. 1 (a) presents the results of oxidized samples and Fig. 1(b) shows the reduced samples which are treated in H_2 at 800 ºC for 3 h, respectively. As shown in Fig. 1, the $NiCr_2O_4$ sample can be determined as pure spinel structure with space group of *I41/amd* and it is fully reduced to Ni and Cr_2O_3 after being exposed to the H_2 atmosphere at 800 ºC for 3 h. Nickel spinel oxides are cubic single phase, while nickel chromite exhibits a tetragonal structure. The characteristic peak of $NiCr_2O_4$ at ~36° appears for chromium oxide-loaded Ni/YSZ, which indicates Cr_2O_3 has reacted with NiO to from $NiCr_2O_4$; however, the peaks of Cr_2O_3 appear after high temperature reduction in H_2 implies that the $NiCr_2O_4$ may be *in situ* reduced to a core-shell structure with Ni metal coated with Cr_2O_3. The spectrum of the oxidized Ni/YSZ, chromium oxide-loaded Ni/YSZ has peaks at ~30°, 35°, 50°, 59° and 63° corresponding to YSZ, as well as peaks at ~37°, 43° and 63° corresponding to NiO. After exposure to H_2, the peaks of NiO disappear and there exist the peaks of Ni confirming NiO has been reduced to Ni. No phase transition is observed in the YSZ even after the high-temperature treatment in a very reducing atmosphere, firmly verifying superior redox stability of the YSZ.

Fig. 2 shows the high-resolution transmission electron microscopy (HR-TEM) analysis of the oxidized and reduced $NiCr_2O_4$, respectively. As shown in Fig. S1 (a), the oxidized $NiCr_2O_4$ has revealed lattice spacing of 0.249(6) nm for (211) and 0.168(7) nm for (312). Fig. 2 shows the TEM images of reduced $NiCr_2O_4$ samples, which confirm that the reduced $NiCr_2O_4$ is mixture of two phases: Cr_2O_3+Ni. It can be observed in Fig. 2, the analysis results for the nickel indicates lattice spacing of 0.176(5) nm (200) and 0.203(1) nm (111), respectively, consistent with the standard data for the nickel. However, the reduction of $NiCr_2O_4$ leads to growth of Cr_2O_3 on Ni surfaces and nickel is coated with Cr_2O_3 nanoparticles, which is similar with the core-shell structure. As shown in Fig. 2 (a2), Ni is surrounded with Cr_2O_3 in the form of heterojunction: the lattice spacing of core Ni is 0.203(1) nm (111) and the interplanar spacing of shell Cr_2O_3 is 0.363(3) nm (012). Fig. 3 shows the SEM maps taken from the oxidized and reduced $NiCr_2O_4$ pellets, respectively. The sintered samples were reduced in 5% H_2/Ar at 800

ºC for 10 h. As shown in Fig. 3 (a), the oxidized sintered $NiCr_2O_4$ pellet is not highly dense, clear images reveal the sample with low sinterability and high porosity; clear crystalline facets with tetrahedral and octahedral structures are observed, indicating the formation of spinel structure. In contrast, the morphology of reduced $NiCr_2O_4$ has been changed significantly: the morphology changes from polyhedral structure to spherical structure, as shown in Fig. 3 (b). Fig. S2 shows the scanning electron micrographs and energy-dispersive X-ray spectroscopy maps taken from the reduced $NiCr_2O_4$ pellets. It can be observed that the Cr_2O_3 nanoparticles are uniformly distributed in the reduced sample and cover the Ni. The TEM and SEM results testify Ni is surrounded with Cr_2O_3 and the Ni@Cr_2O_3 core-shell structure may play an active role in improving carbon deposition resistance of the Ni/YSZ electrode for dry methane reforming.

To confirm the elemental valence change, XPS analysis is performed to test the oxidized and reduced $NiCr_2O_4$ samples. All XPS dates are fitted using a Shirley-type background subtraction method, and the background functions for different spectra of the elements are fitted by 80% Gaussian and 20% Lorenz. Fig. 4 (a1) and (a2) show the Ni 2p core-level XPS results of oxidized and reduced $NiCr_2O_4$, respectively. As shown in Fig. 4 (a1), the Ni^{2+} $2p_{3/2}$ peaks are observed at 853.90, 855.80, 856.50 and 861.30 eV with two shakeup satellites at 861.00 and 864.30 eV; the Ni^{2+} $2p_{1/2}$ peaks are observed at 873.6 eV with a shakeup satellite at 879.90 eV. Generally, pure Ni gives peaks at around 852.30 ($2p_{3/2}$) and 870.00 eV ($2p_{1/2}$), which appear slightly in Fig. 4(a2). Although it is difficult to validate the existence of pure Ni phases in the samples according to the results of XPS, the XRD results have confirmed the presence of a Ni phase. It is reasonable that there are no obvious signals of pure Ni in XPS results when the surface is covered with Cr_2O_3. This is because XPS can only detect signals within the upper 10 nm thickness on the surface, while the XRD can detect signals in micro-order thickness. In Fig. 4 (b1), the Cr^{3+} $2p_{3/2}$ peaks are observed at 575.50, 576.20, 577.00, 578.20 and 579.20 eV; the Cr^{3+} $2p_{1/2}$ peak appears at 585.90 eV. Fig. 4(b2) presents the Cr 2p peaks at binding energies of 575.20, 576.20 and 585.90 eV. The dominant peaks at 576.20 and 585.90 eV can be attributed to Cr_2O_3. O 1s spectra of oxidized and reduced $NiCr_2O_4$ are shown in Fig. S3. The broad peak of O 1s can be fitted with two peaks at binding energies of ~ 530.00 and 531.00 eV. The dominant peak at 530.00 eV is characteristic of oxygen in metal oxides; the other peak at about 531.00 eV indicates that the presence of other components such as OH, H_2O and carbonate species adsorbed on the surfaces. On the one hand, the characteristic peak of oxygen occupies a larger proportion in Fig. S3 (a) than Fig. S3 (b), which is according to the chemical formulas $NiCr_2O_4$ and Cr_2O_3+ Ni, respectively; on the other hand, the other peak has higher proportion in Fig. S3 (b) also suggests H_2O and CO_2 are tend to be adsorbed on the metal oxide surfaces. The better adsorption performances in metal oxide may play a significant role for the electrochemical conversion of H_2O and CO_2 into fuels in the efficient solid oxide electrolysers.

In order to study the electrical properties of $NiCr_2O_4$, conductivity tests were performed in air *versus* temperature (400–800 °C) and oxygen partial pressure (pO_2) at 800 °C. As shown in Fig. 5 (a), the conductivity shows linear behavior with T, over a wide range of temperatures, which is indicative of semiconductor behavior. $NiCr_2O_4$ is normal spinel, with Ni^{2+} cations occupying the tetrahedral sites and Cr^{3+} cations occupying the octahedral sites, though $NiCr_2O_4$ exhibits a tetragonal distortion below 310 K. All oxygen anions within the spinel lattice are bonded to a single tetrahedral cation and three octahedral cations. So the conductivity of $NiCr_2O_4$ is mainly because of the Cr^{3+}-Cr^{3+} direct interaction between octahedral sites, where the transport property rises from hopping of localized *d* electrons between cations [54-55]. The conductivity of $NiCr_2O_4$ decreases with decreasing oxygen partial pressure which is due to that the $NiCr_2O_4$ is reduced to Ni+Cr_2O_3 and Ni is coated with Cr_2O_3 without forming connected Ni network. As observed in Fig. S4, the conductivity of reduced Ni/YSZ and chromium oxide-loaded Ni/YSZ samples display typical metallic behaviors with negative temperature coefficients in 5% H2/Ar, which indicates typical n type conducting mechanism in reducing atmospheres. The conductivity of 5% chromium oxide-loaded Ni/YSZ is considerable with reduced Ni/YSZ which indicates 5% chromium oxide has little effect on the conductivity Ni/YSZ.

Fig. 6 shows the AC impedance of symmetric cells based on Ni/YSZ and 5% Cr_2O_3-Ni/YSZ tested under a series of hydrogen partial pressure at 800 °C. The series resistance of the cell (R_S) corresponds to the first intercept and the difference between the two intercepts is a measure of the electrode polarization resistance (R_p). The Zview software is employed to calculate the R_s and R_p values, as reported in our previous work [56]. The ionic resistance of the YSZ electrolyte, which primarily contributes to the R_s, is typically stable for a wide range of hydrogen partial pressures. The R_p of the symmetric cell based on Ni/YSZ decreased from about 0.80 to 0.50

$\Omega \cdot cm^2$ when the hydrogen partial pressure increased from 10% to 100%, which suggests that a stronger reducing atmosphere is beneficial for improving the electrode polarization. The stronger reducing atmosphere is favorable for the n-type electrical conductivity of the reduced Ni/YSZ and 5% Cr_2O_3-Ni/YSZ samples, which leads to improved electrode performances. In contrast, the R_p of the symmetric cell based on 5% Cr_2O_3-Ni/YSZ decreased from about 1.40 to 1.10 $\Omega \cdot cm^2$ as the hydrogen concentration increased. The R_p of the symmetric cell based on 5% Cr_2O_3-Ni/YSZ is larger than Ni/YSZ, which may be attributed to that Ni is coated with Cr_2O_3 leading to decrease charge transfer and species diffusion in this composite electrode and thereby provides higher resistance. On the other hand, the presence of Cr_2O_3 reduces the conductivity of Ni/YSZ in a certain extent. However, significant change has been observed for the Ni/YSZ and 5% Cr_2O_3-Ni/YSZ composite electrodes in the symmetric cells in a methane atmosphere, with a methane concentration ranging from 5% to 100%, as shown in Fig. 7. In this case, the R_p of the symmetric cell based on Ni/YSZ decreases from approximately 2.60 to 1.75 $\Omega \cdot cm^2$ for a methane concentration range of 5% to 100%, while the R_p value based on 5% Cr_2O_3-Ni/YSZ improved from 2.60 to 1.50 $\Omega \cdot cm^2$ under the same conditions. The R_p values decrease with increasing methane concentration; however, they are still larger than polarization values in hydrogen. This is because of the reducing atmosphere of methane, which is not comparable to hydrogen and sufficient to reduce the cathode with the risk of carbon deposition. The R_p of the symmetric cell based on 5% Cr_2O_3-Ni/YSZ is smaller than the R_p of the symmetric cell based on Ni/YSZ in the methane atmosphere. The results may be due to Ni is coated with Cr_2O_3, which can prevent carbon deposition effectively, possibly by adsorbing the electrochemically produced H_2O or CO_2 from the oxidation of CH_4. Fig. 8 shows the microstructures of the Ni/YSZ and 5% Cr_2O_3-Ni/YSZ electrodes after reducing in CH_4-CO_2 (1:1) atmosphere for 1 h at 800 ºC. As shown in Fig. 8 (a), carbon fibers occur in the Ni/YSZ electrode, however, carbon fibers are not observed in 5% Cr_2O_3-Ni/YSZ electrode. It is found that the 5% Cr_2O_3-Ni/YSZ electrode reveals similar morphology with Fig. 8 (b), suggesting that Cr_2O_3 has covered the Ni particles, which shows the better carbon deposition resistance.

The electrochemical methane reforming is investigated in two types of solid oxide electrolysers with Ni/YSZ and 5% Cr_2O_3-Ni/YSZ cathodes under a series of applied voltages at 800 ºC. Fig. 9 (a) presents the typical curves of the current density as a function of voltage (*I-V* curves) of the electrolyzers for the electrochemical reforming of dry CH_4-CO_2 mixtures. For the Ni/YSZ cathode at 800 ºC, the maximum current density reaches approximately 123 $mA \cdot cm^{-2}$ at 2.0 V, meanwhile, the cell based on 5% Cr_2O_3-Ni/YSZ cathode is improved and the current density reaches about 150 $mA \cdot cm^{-2}$ under the same conditions. As shown in Fig. 9 (b), the current densities increase along with applied voltages, and they are stable at a fixed applied potential, indicating a stable electrochemical process. The current density with the 5% Cr_2O_3-Ni/YSZ cathode reaches approximately 26, 42 and 83 $mA \cdot cm^{-2}$ at 1.2, 1.4 and 1.6 V, respectively, which is higher than 20, 34 and 69 $mA \cdot cm^{-2}$ for the Ni/YSZ electrode under the same conditions. It can be observed that the current densities with the Ni/YSZ electrode decrease obviously in the electrolysis process, which may be due to carbon deposition leading to the loss of the electrical conductivity and degradation of the electrode performances.

Fig. 10 presents the *in situ* AC impedance spectroscopy of cells with Ni/YSZ and 5% Cr_2O_3-Ni/YSZ cathodes in a series of applied voltages ranging from 1.2 to 2.0 V at 800 ºC in 20% CH_4/20% CO_2/60% Ar. It is observed that the R_s values are stabilized at approximately 2.0 $\Omega \cdot cm^2$; however, the R_p values considerably decrease as the applied voltage increase from 1.2 to 2.0 V, which may be attributed to the fact the applied voltage activates the electrodes to the extent that R_p will remarkably decrease and electrochemically reduces the electrode to enhance the mixed conductivity and electrocatalytic activity. Two semicircles are noted on the impedance spectra: the high-frequency arcs (R_1) and low-frequency arcs (R_2). As shown in Table 1, at high-frequency, the R_1 of the solid oxide electrolyzers with cathodes based on Ni/YSZ improves from 2.24 to 0.82 $\Omega \cdot cm^2$ with the applied voltage ranging from 1.2 to 2.0 V. At low-frequency, it is observed that the mass transfer, R_2, dominates the electrode process of the solid oxide electrolysers, which is probably due to the gas conversion, dissociative adsorption and species transfer in the composite electrodes. The R_2 for the cell based on Ni/YSZ cathode remarkably improves from 11.03 to 3.14 $\Omega \cdot cm^2$ with the applied voltage ranging from 1.2 to 2.0 V, suggesting the improved kinetics of gas conversion at high voltages. By contrast, R_1 and R_2 for the cell based on the 5% Cr_2O_3-Ni/YSZ cathode significantly decreases to 1.90 and 9.32 at low voltages and is further enhanced to 0.28 and 2.54 $\Omega \cdot cm^2$ at high voltages, respectively, which indicates that Cr_2O_3 may have

covered the surface of Ni and thereby reduced the activity of Ni for CH_4 cracking reaction and carbon deposition; on the other hand, it may be attributed to the improved mass transfer because of the chemical adsorption of CO_2 or CH_4 on the surface of Cr_2O_3.

Fig. 11 shows the short term performances of electrochemical methane reforming in solid electrolysers based on Ni/YSZ and 5% Cr_2O_3-Ni/YSZ cathodes. As shown in Fig. 11, the conversion of CH_4 and CO_2 are 51% and 30% for Ni/YSZ cathode under an open circuit at 800 °C. The conversion of CH_4 and CO_2 reaches 53% and 37% for the cell based on the 5% Cr_2O_3-Ni/YSZ cathode under the same condition. It is shown that CH_4 and CO_2 have different conversions suggesting that the methane reforming reaction is not simple. The reforming of CH_4 with CO_2 is a dominant reaction ($CH_4 + CO_2 \rightarrow 2CO + 2H_2$) in the electrochemical methane reforming in solid oxide electrolysers [57-58]. However, reverse water gas shift reaction ($CO_2 + H_2 \leftrightarrow CO + H_2O$) occurs at the same time which will change the carbon oxide conversion and the production of H_2 and CO [59-60]. In the meantime, methane cracking ($CH_4 \rightarrow C(s) + 2H_2$) may happens and produces carbon which will lead to carbon deposition on the Ni particles, deactivation of the cathode and performance loss of the cell, while the CO disproportionation reaction ($2CO \rightarrow C(s) + CO_2$) probably take place [61-62]. Meanwhile, the steam/carbon gasification ($C + H_2O \rightarrow CO + H_2$) also may occur. However, the Sabatier reaction ($CO_2 + 4H_2 \rightarrow CH_4 + 2H_2O$, $CO + 3H_2 \rightarrow CH_4 + H_2O$) may be negligible which is attributed to the high temperature [63-64]. These secondary reactions are expected to change the conversion of methane and carbon dioxide. It can be seen in Fig. 11, the conversion of CH_4 and CO_2 increases along with the applied voltages suggesting that applied voltages remarkably promote the methane reforming. For the Ni/YSZ cathode, the maximum conversions of CH_4 and CO_2 are approximately 59% and 47% at 1.6 V at 800 ºC, which improved by approximate 20% for CH_4 conversion and more than 50% for CO_2 conversion compared with the values without applied voltages. However, the conversions of CH_4 and CO_2 are higher with the 5% Cr_2O_3-Ni/YSZ cathode, which further indicates impregnated chromium oxide in the Ni/YSZ cathode has enhanced the performances of electrode and carbon deposition resistance.

Fig. 12 shows the rate of H_2 and CO production from methane reforming in the cell based on Ni/YSZ and 5% Cr_2O_3-Ni/YSZ cathodes under a series of applied voltages at 800 ºC. It is observed that the yields of H_2 and CO accordingly increase with applied voltage increasing from 0 to 1.6 V. Higher applied voltages can produce stronger reducing conditions in the cathode and further activate the electrode for electrochemical methane reforming. The carbon dioxide can be electrochemically split into oxide ion and carbon monoxide in the cathode and then a part of oxide ion can be *in situ* utilized to electrochemically oxidize methane and generates syngas ($CO_2 + 2e^- \rightarrow CO + O^{2-}$, $CH_4 + O^{2-} \rightarrow CO + H_2 + 2e^-$). As shown in Fig. 12, the maximum H_2 production for the cell based on the 5% Cr_2O_3-Ni/YSZ electrode is approximately 2.4 ml min^{-1} cm^2, which is higher than 1.9 ml min^{-1} cm^2 at 1.6 V with the Ni/YSZ cathode. The CO productions are 2.0 and 1.6 ml min^{-1} cm^2 at 1.6 V for the cells based on 5% Cr_2O_3-Ni/YSZ and Ni/YSZ cathodes, respectively. The different productions between H_2 with CO also indicate that the reaction of electrochemical methane reforming is not single. Dry CO_2 reforming of methane produces a syngas with a H_2-CO ratio 1:1; meanwhile, water gas shift reaction, CH_4 decomposition, CO disproportionation reaction, the steam/carbon gasification and the Sabatier reaction occur, which will influence the final conversion of CH_4 and CO_2 as well as the production of H_2 and CO.

Conclusions

In this work, direct electrochemical methane reforming is demonstrated in an oxide-ion-conducting solid oxide electrolyser with Ni/YSZ cathode. At the same time, the effect of Cr_2O_3 loading into the Ni/YSZ cathode is studied in terms of carbon accumulation and electrochemical performance in symmetric cells and electrolysis cells. Cr_2O_3 is impregnated in Ni/YSZ electrode to form $NiCr_2O_4$ and then reduced to *in situ* construct a core-shell structure with Ni metal core coated with Cr_2O_3 surface which leads to a decrease in performances in H_2, however, an increase in performances during tests in CH_4 results in low polarization resistance and better carbon deposition resistance. Efficient dry reforming of CH_4-CO_2 is successfully achieved in Ni/YSZ cathode under applied voltages. Higher conversion of CH_4 and CO_2 from the *in situ* electrochemical methane reforming with 5% Cr_2O_3-Ni/YSZ cathode is achieved. The improved performances may be attributed to the formation of Cr_2O_3 on Ni surface with heterojunction interface, which may improve the CO_2 chemical adsorption and carbon deposition resistance.

Acknowledgements

This work is supported by the Natural Science Foundation of China (No. 21303037).

Notes and references

[a] School of Materials Science and Engineering, Hefei University of Technology, No.193 Tunxi Road, Hefei, Anhui 230009, China.
[b] Fujian Institute of Research on the Structure of Matter, Chinese Academy of Sciences, 155 Yangqiao Road West, Fuzhou, 350002, China
*Corresponding: kxie@fjirsm.ac.cn

† Footnotes should appear here. These might include comments relevant to but not central to the matter under discussion, limited experimental and spectral data, and crystallographic data.
Electronic Supplementary Information (ESI) available: [details of any supplementary information available should be included here]. See DOI: 10.1039/b000000x/

1 S. Sista, Z. Hong, L.M. Chen, Y. Yang, *Energy Environ. Sci.*, 2011, 4, 1606-1620

2 A. Hauch, S.D. Ebbseen, S.H. Jensen, M. Mogensen, *J. Mater. Chem.*, 2008, 18, 2331-2340

3 K. Tomishige, T. Miyazawa, M. Asadullah, S. Ito, K. Kunimori, *Green Chem.*, 2003, 5, 399-403

4 R. Bouarab, O. Cherifi, A. Auroux, *Green Chem.*, 2003, 5, 209-212

5 P. Tang, Q. J. Zhu, Z. X. Wu and D. Ma, *Energy Environ. Sci.*, 2014, 7, 2580–2591

6 B.S. Liu, L. Li, C.T. Au, A.S.C. Cheung, *Catal. Lett.*, 2006, 108, 37-44

7 X. S. Wu, S. Kawi, *Energy Environ. Sci.*, 2010, 3, 334–342

8 B.S. Liu, C.T. Au, *Catal. Lett.*, 2003, 85, 165-170

9 C. Jin, C. H. Yang, F. Zhao, A. Coffin and F. L. Chen, *Electrochem. Commun.*, 2010, 12, 1450–1452

10 J. Wei and E. Iglesia, *J. Catal.*, 2004, 224, 370–383

11 Y. Akinaga, T. Taketsugu, K. Hirao, *J. Chem. Phys.*, 1997, 107, 415-424

12 A. Kokalj, N. Bonini, C. Sbraccia, S. Gironcoli, S. Baroni, *J. Am. Chem. Soc.*, 2004,126, 16732-16733

13 R.G. Copperthwaite, P.R. Davies, M.A. Morris, M.W. Roberts, R.A. Ryder, *Catal. Lett.*, 1988, 1, 11-19

14 S.G. Wang, D.B. Cao, Y.W. Li, J.G. Wang, H.J. Jiao, *J. Phys. Chem. B*, 2005, 109, 18956–18963

15 G. Tsekouras, D. Neagu and J. T. S. Irvine, *Energy Environ. Sci.*, 2013, 6, 256–266

16 M. Ni, M. K. H. Leung and D. Y. C. Leung, *Int. J. Hydrogen Energy*, 2008, 33, 2337–2354

17 T. Ishihare, N. Jirathiwathanakul, H. Zhong, *Energy Environ. Sci.*, 2010, 3, 665-672.

18 P. Aguiar, D. Chadwick, L. Kershenbaum, *Chem. Eng. Sci.*, 2002, 57, 1665-1677

19 W. T. Qi, Y. Gan, D. Yin, Z. Y. Li, G. J. Wu, K. Xie and Y. C. Wu, *J. Mater. Chem. A*, 2014, 2, 6904-6915

20 Y. X. Li, Y. Gan, S. S. Li, Y. Wang, H. F. Xiang and K. Xie, *Phys. Chem. Chem. Phys.*, 2012, 14, 15547–15553

21 K. R. Sridhar and B. T. Vaniman, *Solid State Ionics*, 1997, 93, 321–328

22 K. Xie, Y. Q. Zhang, G. Y. Meng and J. T. S. Irvine, *Energy Environ. Sci.*, 2011, 4, 2218–2222

23 C. Graves, S.D. Ebbesen, M. Mogensen, *Solid State Ionics*, 2011, 192, 398-403

24 S. D. Ebbesen, M. Mogensen, *J. Power Sources*, 2009, 193, 349-358

25 H. Koide, Y. Someya, T. Yoshida, T. Maruyama, *Solid State Ionics*, 2000, 132, 253-260

26 E.S. Hecht, G.K. Gupta, H.Y. Zhu, A.M. Dean, R.J. Kee, L. Maier, O. Deutschmann, *Appl. Catal. A*, 2005, 295, 40-51

27 D. Neagu and J. T. S. Irvine, *Chem. Mater.*, 2010, 22, 5042–5053

28 A. Ghosh, A. K. Azad and J. T. S. Irvine, *ECS Trans.*, 2011, 35, 1337–1343

29 H. He and J. M. Hill, *Appl. Catal. A*, 2007, 317, 284-292

30 J.H. Koh, Y.S. Yoo, J.-W. Park and H. C. Lim, *Solid State Ionics*, 2002, 149, 157-166

31 A.L. Dicks, *J. Power Sources*,1998, 71, 111-122

32 K.C. Wincewicz, J.S. Cooper, *J. Power Sources*, 2005,140, 280-296

33 C. Guerra, A. Lanzini, P. Leone, M. Santarelli, N.P. Brandon, *J. Power Sources*, 2014, 245, 154-163

34 Z.Y. Hou, O. Yokota, T. Tanaka, T. Yashima, *Catal. Lett.*, 2003, 87, 37-42

35 M.C.J. Bradford, M.A. Vannice, *Catal. Lett.*, 1997, 48, 31-38

36 S. Tao and J. T. S. Irvine, *J. Electrochem. Soc.*, 2004, 151, A252-A259

37 S. Lee, G. Kim, J. M. Vohs and R. J. Gorte, *J. Electrochem. Soc.*, 2008, 155, B1179-B1183

38 Y.H. Huang, R. I. Dass, Z.L. Xing and J. B. Goodenough, *Science*, 2006, 312, 254-257

39 S. W. Tao, J. T. S. Irvine, *Nat. Mater.*, 2003, 2, 320-323

40 Q.Q. Qin, K. Xie, H.S. Wei, W.T. Qi, J.W Cui, Y.C. Wu, *RSC Adv.*, 2014, 4, 38474-38483

41 E. Nikolla, J. Schwank and S. Linic, *Catal. Today*, 2008, 136, 243-248

42 S.I. Lee, J. M. Vohs and R. J. Gorte, *J. Electrochem. Soc.*, 2004, 151, A1319-A1323

43 H. Sumi, Y.H. Lee, H. Murovama, T. Matsui, K. Eguchi, 2010, *J. Electrochem. Soc.*,157, B1118-B1125

44 J.T. Zhang, F.L. Liang, B. Chi, J. Pu and L. Jian, *J. Power Sources*, 2012, 200, 29-33

45 S. Park, J. M. Vohs and R.J. Gorte, *Nature*, 2000, 404, 265-267

46 S. Park, R. Craciun, J.M. Vohs and R.J. Corte, *J. Electrochem. Soc.*, 1999, 146, 3603-3605

47 M.D. Gross, J.M. Vohs, R.J. Gorte, *Electrochim. Acta*, 2007, 52, 1951-1957

48 L. Yang, Y. Choi, W. Qin, H. Chen, K. Blinn, M. Liu, P. Liu, J. Bai, T. A. Tyson and M. Liu, *Nat. Commun.*, 2011, 2, 357, DOI: 10.1038/ncomms1359

49 J. M. Serra and W. A. Meulenberg, J. Am. Ceram. Soc., 2007, 90, 2082-2089

50 M. Liu, Y. Choi, L. Yang, K. Blinn, W. Qin, P. Liu and M. Liu, *Nano. Energy*, 2012, 1, 448–455

51 S.B. Wang, K. Murata, T. Hayakawa, S. Hamakawa, K. Suzuki, *Catal. Lett.*, 1999, 63, 59-64

52 J. El-Idrissi, M. Kacimi, F. Bozon-Verduraz and M. Ziyad, *Catal. Lett.*, 1998, 56, 221-225

53 L.A. Chick, L.R. Pederson, G.D. Maupin, J.L. Bates, L.E. Thomas, G.J. Exarhos, *Mater. Lett.*, 1990, 10, 6-12

54 F. Braestrup, K.K. Hansen, *J. Solid State Electr.*, 2010, 14, 157-166

55 A. Yaresko, V. Antonov, *J. Magn. Magn. Mater.*, 2007, 310, 1672-1674

56 Y. X. Li, Y. Gan, Y. Wang, K. Xie and Y. C. Wu, *Int. J. Hydrogen Energy*, 2013, 38, 10196–10207

57 S. Wang and G. Q. (Max) Lu, *Energy Fuels*, 1996, 10, 896–904

58 A. P. E. York, J. B. Claridge, A. J. Brungs, S. C. Tsang and M. L. H. Green, *Chem. Commun.*, 1997, 39-40

59M. Wisniewski, A. Bor´eave and P. G´elin, *Catal. Commun.*, 2005, 6, 596–600

60 H. Timmermann, D. Fouquet, A. Weber, E. Ivers-Tiff˝ee, U. Hennings and R. Reimert, *Fuel Cells*, 2006, 6, 307–313

61 M. Ando, Y. Hirata, S. Sameshima and N. Matsunaga, *J. Ceram. Soc. Jpn.*, 2011, 119, 794–800

62 S. Assabumrungrat, N. Laosiripojana and P. Piroonlerkgul, *J. Power Sources*, 2006, 159, 1274–1282

63 S. K. Hoekman, A. Broch, C. Robbins and R. Purcell, *Int. J. Greenhouse Gas Control*, 2010, 4, 44–50.

64 K. R. Thampi, J. Kiwi and M. Gr¨atzel, *Nature*, 1987, 327, 506–508

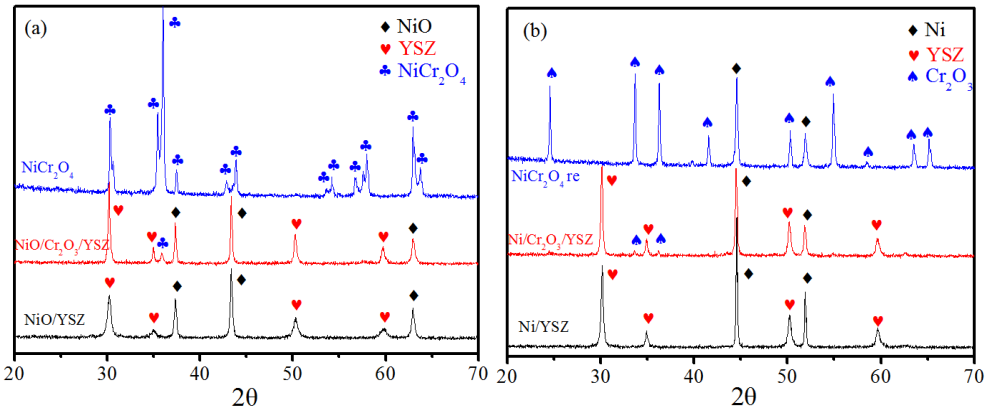

Fig. 1: XRD pattern of Ni/YSZ, Ni/Cr_2O_3/YSZ and $NiCr_2O_4$ (a: the patterns of the oxidized form; b: the patterns of the reduced form).

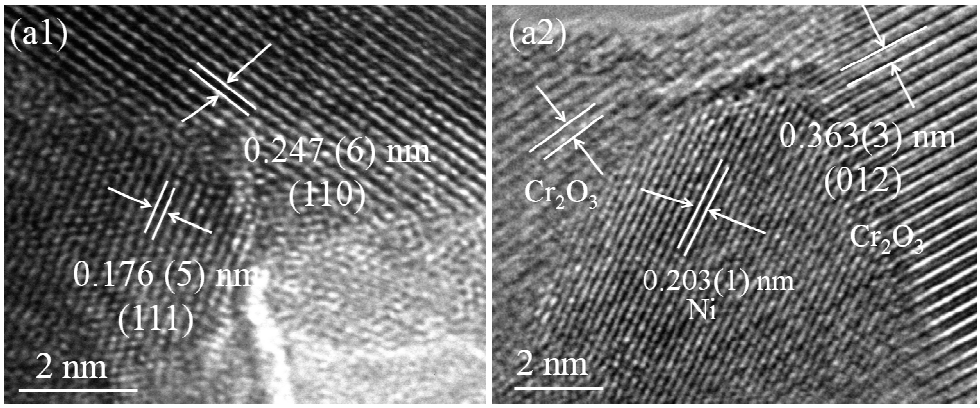

Fig. 2: The TEM graph of the reduced $NiCr_2O_4$ (a1) and (a2).

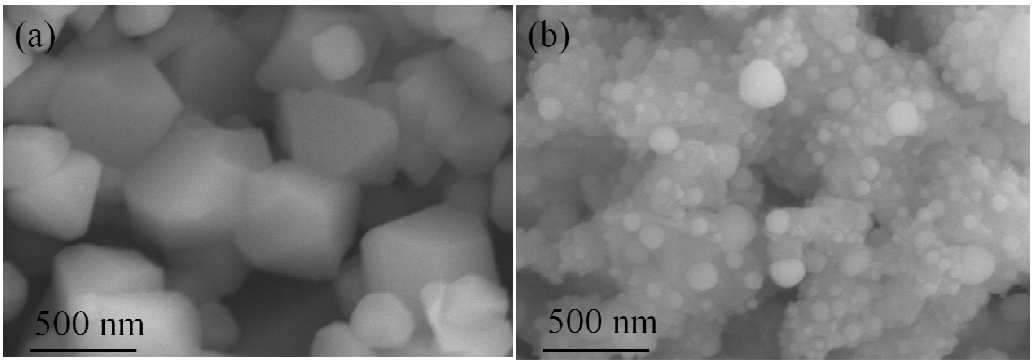

Fig. 3: SEM results of the oxidized form of $NiCr_2O_4$ (a) and the reduced form of $NiCr_2O_4$ (b).

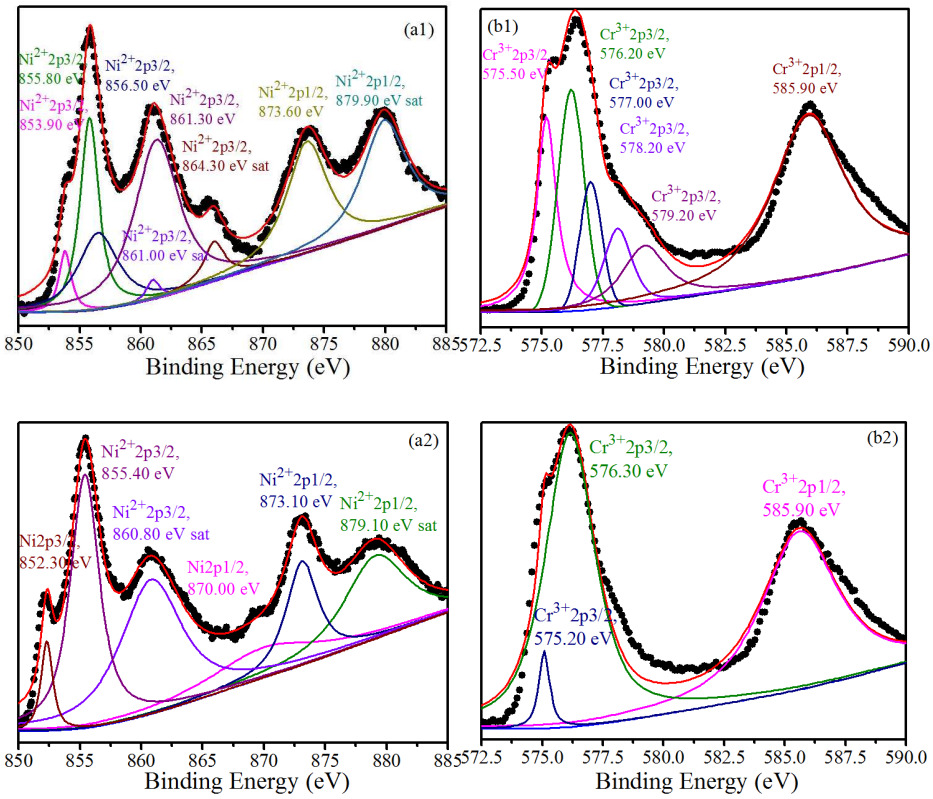

Fig. 4: XPS results of Ni (a1) and Cr (b1) in the oxidized $NiCr_2O_4$; (a2) and (b2) in the reduced $NiCr_2O_4$.

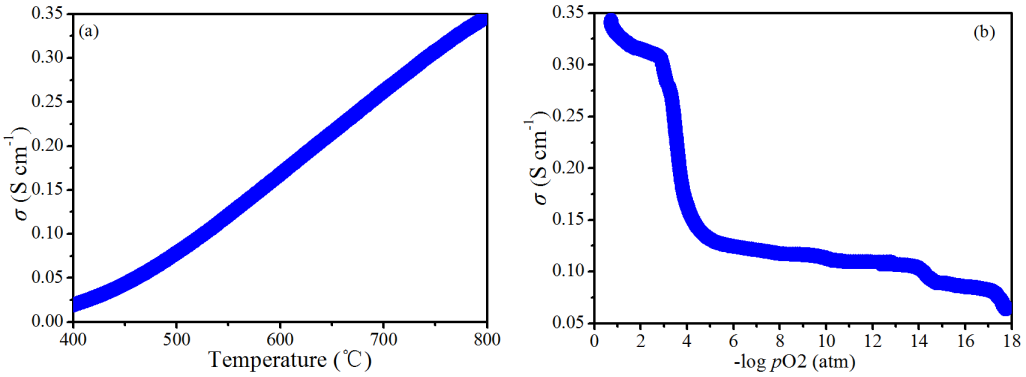

Fig. 5: (a) The dependence of conductivity on temperature of the oxidized form of $NiCr_2O_4$ samples; (b) the dependence of the conductivity on oxygen partial pressure of the oxidized form of $NiCr_2O_4$ samples at 800 ^oC.

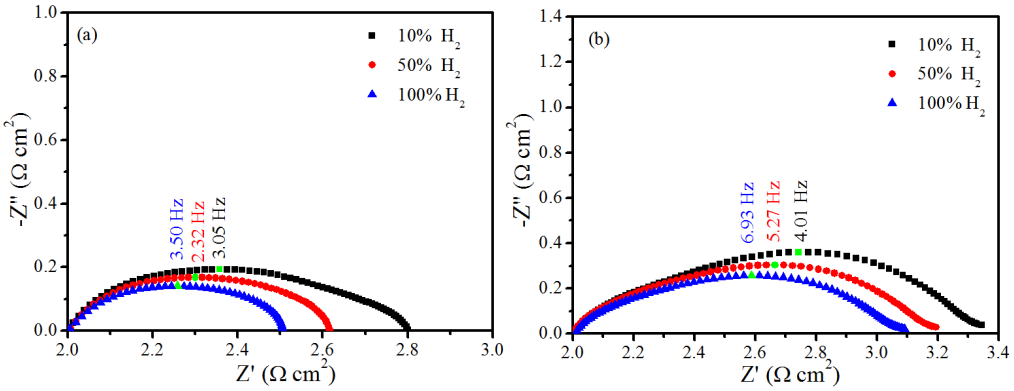

Fig. 6: AC impendence of the symmetrical cells based on Ni/YSZ electrode (a) and 5% Cr_2O_3-Ni/YSZ electrode tested at 800 ^oC with different H_2 partial pressures.

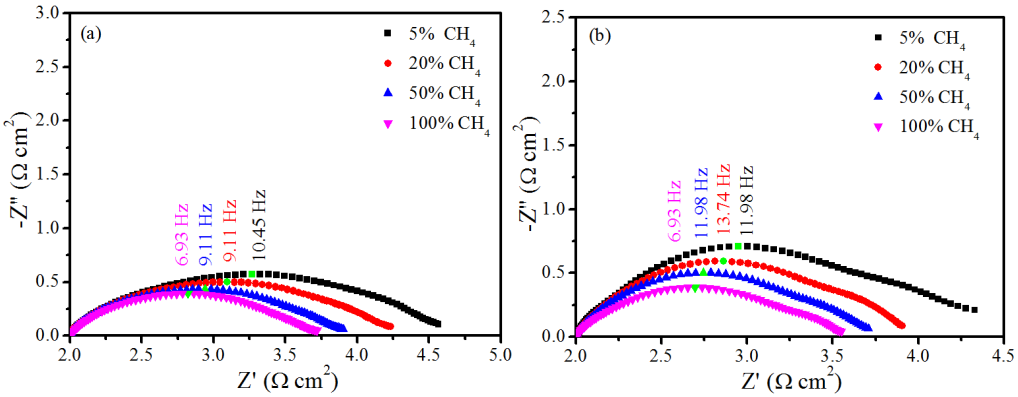

Fig. 7: AC impendence of the symmetrical cells based on Ni/YSZ electrode (a) and 5% Cr_2O_3-Ni/YSZ electrode tested at 800 ^oC with different CH_4 partial pressures.

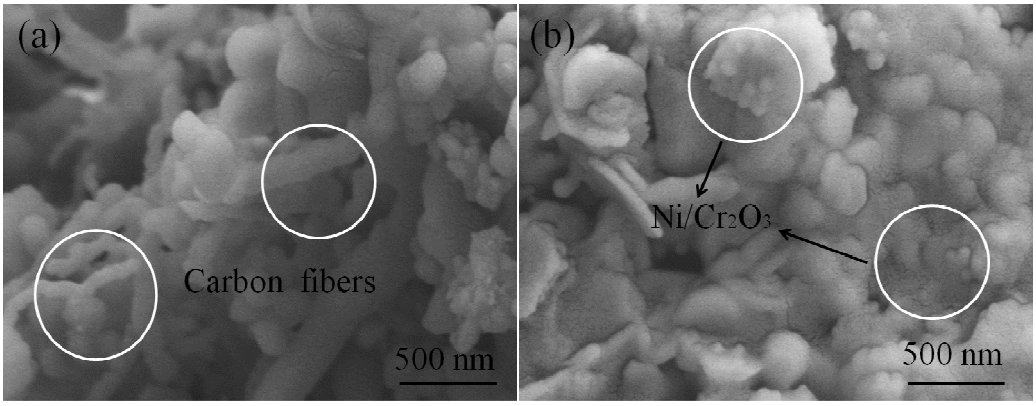

Fig. 8: The microstructures of the Ni/YSZ (a) and 5% Cr_2O_3-Ni/YSZ (b) electrodes after reducing in CH_4-CO_2 (1:1) atmosphere for 1 h at 800 ºC.

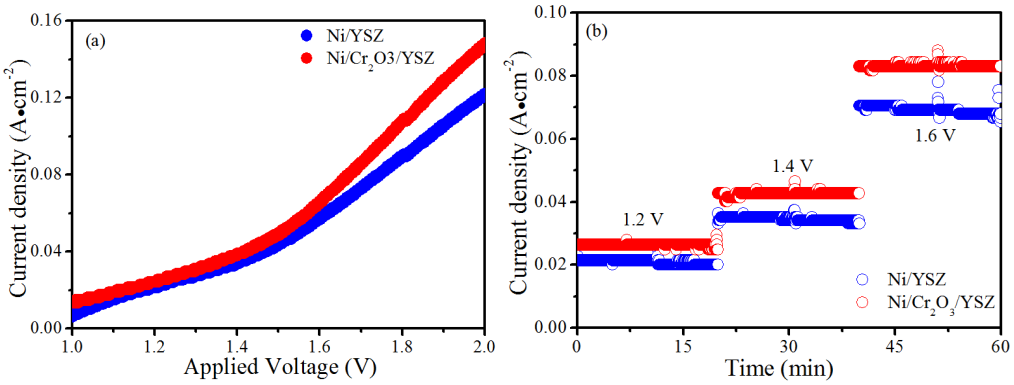

Fig. 9: I-V curve of the solid oxide electrolyzers based on Ni/YSZ and 5% Cr_2O_3-Ni/YSZ cathodes for electrolysisat 800 ^oC.

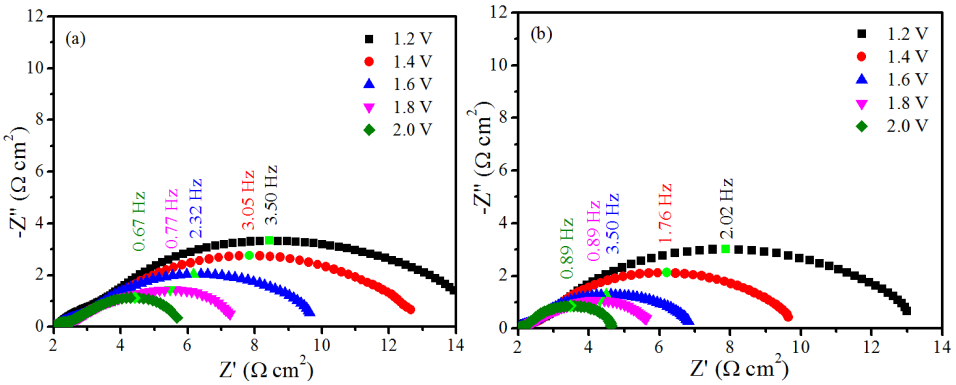

Fig. 10: AC impendence of the solid oxide electrolyzers based on Ni/YSZ (a) and 5% Cr_2O_3-Ni/YSZ (b) for electrolysis at 800 ^oC.

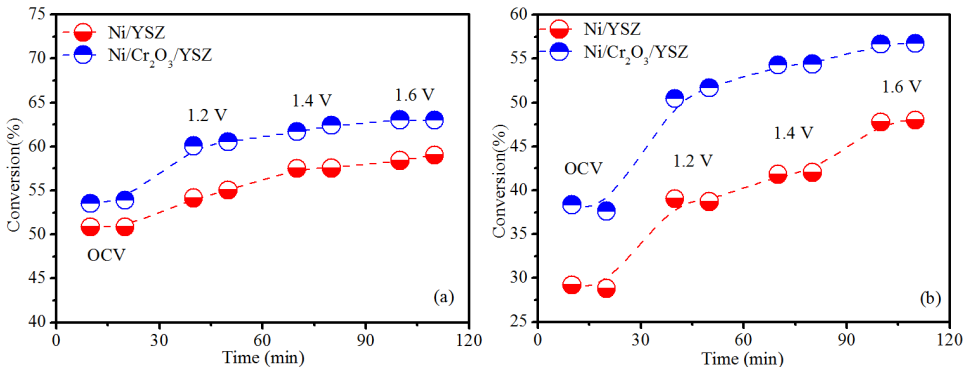

Fig. 11: The conversion of CH_4 (a) and CO_2 (b) based on Ni/YSZ and based on 5% Cr_2O_3-Ni/YSZ in the flow of 20% CH_4/20% CO_2/60% Ar at 800 ^oC.

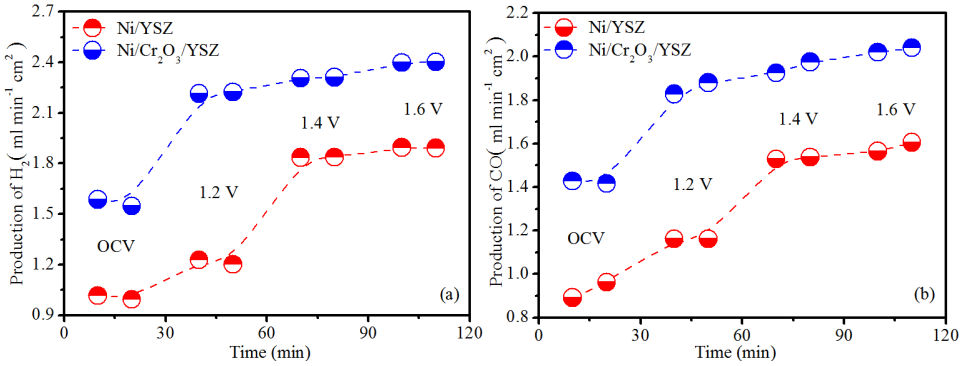

Fig. 12: (a) The production of H_2 , (b) the production of CO based on Ni/YSZ and 5% Cr_2O_3-Ni/YSZ in the flow of 20% CH_4/20% CO_2/60% Ar at 800 ^oC.

Table 1 The R_1 and R_2 of the Ni/YSZ and 5% Cr_2O_3-Ni/YSZ cathodes in the flow of 20% CH_4/20% CO_2/60% Ar at 800 ^oC under various applied voltages.

cathode	Applied Voltages (V)	R_1 ($\Omega \cdot cm^2$)	R_2 ($\Omega \cdot cm^2$)
Ni/YSZ	1.2	2.24	11.03
	1.4	1.98	9.03
	1.6	1.70	6.28
	1.8	1.36	4.39
	2.0	0.82	3.14
5% Cr_2O_3-Ni/YSZ	1.2	1.90	9.32
	1.4	1.56	6.44
	1.6	0.98	4.02
	1.8	0.56	3.28
	2.0	0.28	2.54